

## A magnonic directional coupler for integrated magnonic half-adders

Wang, Q.; Kewenig, M.; Schneider, M.; Verba, R.; Kohl, F.; Heinz, B.; Geilen, M.; Mohseni, M.; Cotofana, S. D.; More Authors

**DOI**

[10.1038/s41928-020-00485-6](https://doi.org/10.1038/s41928-020-00485-6)

**Publication date**

2020

**Document Version**

Final published version

**Published in**

Nature Electronics

**Citation (APA)**

Wang, Q., Kewenig, M., Schneider, M., Verba, R., Kohl, F., Heinz, B., Geilen, M., Mohseni, M., Cotofana, S. D., & More Authors (2020). A magnonic directional coupler for integrated magnonic half-adders. *Nature Electronics*, 3(12), 765-774. <https://doi.org/10.1038/s41928-020-00485-6>

**Important note**

To cite this publication, please use the final published version (if applicable).  
Please check the document version above.

**Copyright**

Other than for strictly personal use, it is not permitted to download, forward or distribute the text or part of it, without the consent of the author(s) and/or copyright holder(s), unless the work is under an open content license such as Creative Commons.

**Takedown policy**

Please contact us and provide details if you believe this document breaches copyrights.  
We will remove access to the work immediately and investigate your claim.



# A magnonic directional coupler for integrated magnonic half-adders

Q. Wang<sup>1,2</sup>✉, M. Kewenig<sup>2</sup>, M. Schneider<sup>1,2</sup>, R. Verba<sup>3</sup>, F. Kohl<sup>2</sup>, B. Heinz<sup>1,2,4</sup>, M. Geilen<sup>2</sup>, M. Mohseni<sup>2</sup>, B. Lagel<sup>5</sup>, F. Ciubotaru<sup>6</sup>, C. Adelmann<sup>1,6</sup>, C. Dubs<sup>1,7</sup>, S. D. Cotofana<sup>1,8</sup>, O. V. Dobrovolskiy<sup>1</sup>, T. Bracher<sup>2</sup>, P. Pirro<sup>1,2</sup> and A. V. Chumak<sup>1,2</sup>✉

**Magnons, the quanta of spin waves, could be used to encode information in beyond-Moore computing applications, and magnonic device components, including logic gates, transistors and units for non-Boolean computing, have already been developed. Magnonic directional couplers, which can function as circuit building blocks, have also been explored, but have been impractical because of their millimetre dimensions and multimode spectra. Here, we report a magnonic directional coupler based on yttrium iron garnet that has submicrometre dimensions. The coupler consists of single-mode waveguides with a width of 350 nm. We use the amplitude of a spin wave to encode information and to guide it to one of the two outputs of the coupler depending on the signal magnitude, frequency and the applied magnetic field. Using micromagnetic simulations, we also propose an integrated magnonic half-adder that consists of two directional couplers and we investigate its functionality for information processing within the magnon domain. The proposed half-adder is estimated to consume energy in the order of attojoules.**

Spin waves (and their quanta magnons) in magnetic structures could potentially be used as data carriers in future low-energy computing devices<sup>1–5</sup>. Spin waves can transfer information with low losses<sup>1–4,6,7</sup> and can be used to implement logic functionality based on a wide range of nonlinear spin-wave phenomena<sup>8–10</sup>. The phase of a coherent spin wave provides an additional degree of freedom (beyond amplitude) in data processing, thus decreasing the footprint of logic units<sup>11–13</sup>, and magnonic structures can be scaled down to the nanometre regime<sup>14,15</sup> and use spin waves with nanometre wavelengths<sup>16–18</sup>. Nanoscale single-mode magnonic waveguides can also overcome the issue of parasitic magnon scatterings into higher modes<sup>19</sup>. Furthermore, reducing the dimensions of magnonic structures to the atomic scale could potentially shift the frequency of the spin waves from the GHz to the THz range<sup>20,21</sup>.

Several magnon-based data-processing devices have already been demonstrated, including spin-wave logic gates<sup>11,22–25</sup>, majority gates<sup>26,27</sup>, magnon transistors and valves<sup>8,28</sup>, spin-wave multiplexers<sup>29,30</sup> and unconventional and neuromorphic computing elements<sup>31–33</sup>. However, an integrated all-magnonic circuit, which is suitable for the cascading of multiple magnonic units, has not yet been developed. Nanoscale spin-wave directional couplers with reconfigurable functionality can constitute the core of integrated all-magnonic circuits<sup>34</sup>. However, while spin-wave directional couplers have been explored experimentally<sup>35</sup>, their millimetre dimensions and multimode spectrum limit their practical implementation.

In this Article, we report a magnonic directional coupler with single-mode waveguides of submicrometre width and based on yttrium iron garnet (YIG). Using space-resolved micro-focused Brillouin light scattering ( $\mu$ BLS) spectroscopy<sup>36</sup>, we investigate its functionality as a building block for integrated magnonic circuits.

In the linear regime, the directional coupler exhibits the functionality of a microwave filter for the processing of analogue and digital information, a power splitter for fan-out logic gates and a frequency divider or signal multiplexer. In the nonlinear regime, the outputs of the directional coupler can be controlled by varying the spin-wave amplitude, which can be useful for logic gates. We also combine linear and nonlinear directional couplers numerically to construct a half-adder—a prototype of a magnonic integrated circuit. Numerical benchmarking of the proposed half-adder (based on 30-nm technology) against a 7-nm complementary metal-oxide-semiconductor (CMOS) half-adder shows that the proposed device has a 10-fold lower energy consumption and a comparable device footprint.

## Magnonic directional coupler structure

Our submicrometre directional coupler (Fig. 1a) was fabricated from an 85-nm-thick YIG film<sup>6,7</sup> (Methods) and consists of two spin-wave waveguides with a width of 350 nm. Near the point of spin-wave excitation, the waveguides are physically separated by a narrow gap of 320 nm. To transfer spin waves out of the coupled waveguides into an ‘isolated’ conduit, the waveguides bend at an angle of 12° until achieving a gap of 1.32  $\mu$ m. A U-shaped antenna is placed on top of the first YIG waveguide to excite spin waves and at a distance of 2  $\mu$ m to the second waveguide to avoid spin-wave excitation in both waveguides (Extended Data Fig. 1 and Supplementary Note 1). When a field of 56 mT is applied along the waveguides, spin-wave frequencies ranging from 3.4 GHz to 3.63 GHz are excited well by the U-shaped antenna in the first waveguide (Extended Data Fig. 2 and Supplementary Note 2). Only the first width mode can be excited in this frequency range (single-mode nano-waveguide), as shown in the dispersion curve in Fig. 1b. To detect the spin-wave

<sup>1</sup>Faculty of Physics, University of Vienna, Vienna, Austria. <sup>2</sup>Fachbereich Physik and Landesforschungszentrum OPTIMAS, Technische Universitat Kaiserslautern, Kaiserslautern, Germany. <sup>3</sup>Institute of Magnetism, Kyiv, Ukraine. <sup>4</sup>Graduate School Materials Science in Mainz, Mainz, Germany. <sup>5</sup>Nano Structuring Center, Technische Universitat Kaiserslautern, Kaiserslautern, Germany. <sup>6</sup>Imec, Leuven, Belgium. <sup>7</sup>INNOVENT e.V., Technologieentwicklung, Jena, Germany. <sup>8</sup>Department of Quantum and Computer Engineering, Delft University of Technology, Delft, The Netherlands.

✉e-mail: [qi.wang@univie.ac.at](mailto:qi.wang@univie.ac.at); [andrii.chumak@univie.ac.at](mailto:andrii.chumak@univie.ac.at)

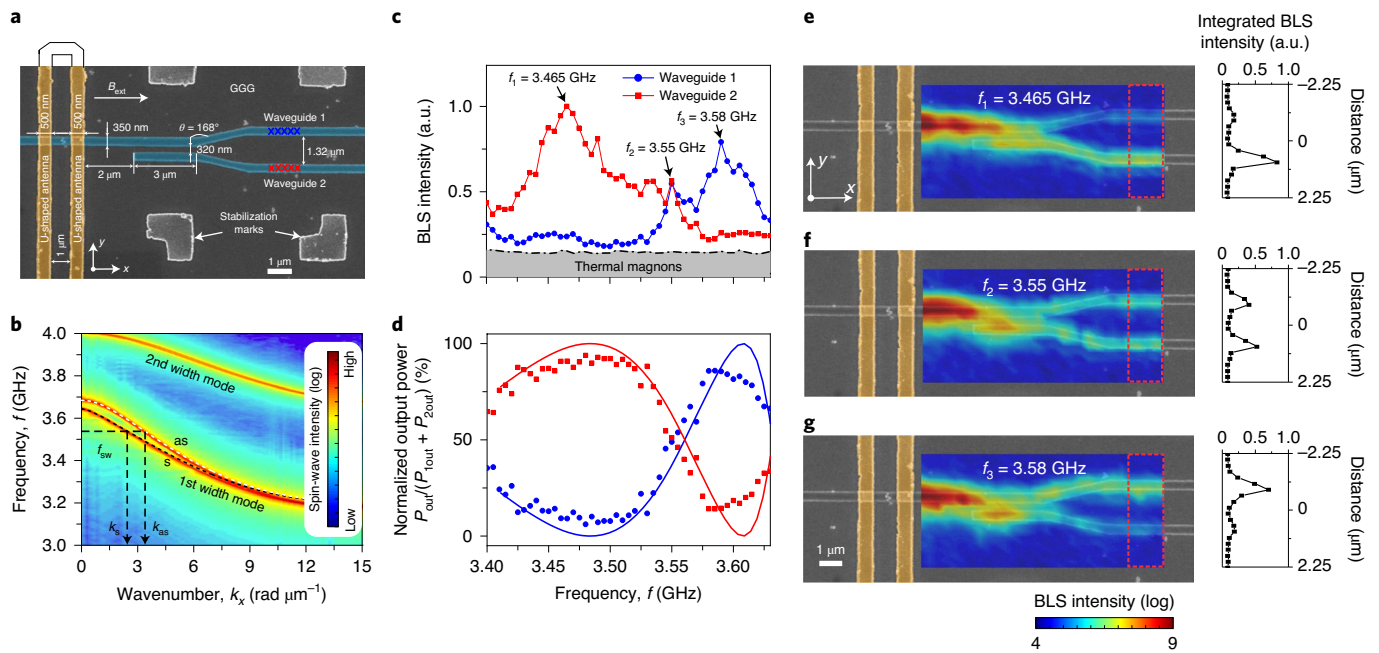


**Fig. 1 | Sample geometry and working principle of the directional coupler in the linear regime.** **a**, Scanning electron microscopy (SEM) image of the directional coupler (shaded in blue) with the U-shaped antenna. An external magnetic field,  $B_{\text{ext}} = 56$  mT, is applied along the YIG conduits ( $x$  axis) to saturate the directional coupler in a backward volume geometry<sup>34</sup> and a radiofrequency (RF) current with power  $P_{\text{mw}} = 0$  dBm is applied to the antenna to excite spin waves. GGG, gadolinium gallium garnet. **b**, Spin-wave dispersion relation of the first two width modes obtained using micromagnetic simulation (colour-coded) and analytic theory (dashed lines). YIG waveguides of 350-nm width and with a 320-nm gap between are considered. **c**, Averaged spin-wave spectra measured by  $\mu$ BLS spectroscopy on the first (blue circles) and second (red squares) output waveguides. The arrows indicate the frequencies chosen for the demonstration of different functionalities of the directional coupler in **e–g**. **d**, The frequency dependence of the normalized output powers  $P_{\text{out}}/(P_{\text{out}} + P_{\text{2out}})$  with subtracted thermal background for both waveguides. Circles and squares represent experimental results and solid lines are theoretical calculations of the normalized output spin-wave intensity at the first (blue) and second (red) output waveguides. **e–g**, Two-dimensional (2D) BLS maps (the laser spot was scanned over an area of  $9.4 \times 4.5 \mu\text{m}^2$  with  $30 \times 20$  points) of the BLS intensity for  $f_1 = 3.465$  GHz (**e**),  $f_2 = 3.55$  GHz (**f**) and  $f_3 = 3.58$  GHz (**g**). The right panels show the spin-wave intensity integrated over the red dashed rectangular regions at the end of the directional coupler.

intensity in the directional coupler, space-resolved  $\mu$ BLS spectroscopy was used (Methods)<sup>36</sup>.

### Linear functionality

As a first step, we measured the spin-wave intensity at five points along each output waveguide, as marked by blue and red crosses in Fig. 1a. Figure 1c shows the spin-wave intensities for the two output waveguides averaged over these points as a function of the excitation frequency. It can be seen that the two spectra show quite different features. In the first waveguide, the maximum spin-wave intensity is observed at 3.58 GHz. By contrast, the maximum intensity in the second waveguide is found around 3.465 GHz, and only very weak spin-wave intensities are detected above 3.575 GHz. To understand the nature of this frequency separation, the dispersion relations of the first two spin-wave width modes for coupled waveguides are shown in Fig. 1b (Methods). The colour coding represents the results of micromagnetic simulations, whereas the dashed lines were calculated using analytical theory (Methods)<sup>15,19</sup>. The dispersion curve of the first width mode splits into antisymmetric (as) and symmetric (s) modes due to the dipolar interaction between the waveguides. This results in an oscillation of the spin-wave energy between the coupled waveguides<sup>19,35</sup>. Thus, once the spin-wave energy is injected into only one of the waveguides, it will be transferred entirely to the other one after propagation through a certain distance, known as the coupling length  $L$ . This is defined by the wavenumbers of the spin-wave modes  $k_{\text{as}}$  and  $k_{\text{s}}$ ,  $L = \pi/\Delta k = \pi/|k_{\text{as}} - k_{\text{s}}|$ , and depends strongly on the spin-wave frequency and other parameters<sup>19</sup>.

Because the length of the coupled waveguides is fixed, the ratio of this length to the coupling length  $L$  defines in which of the two output waveguides of the directional coupler the spin wave is guided. Figure 1d shows the frequency dependence of the normalized output spin-wave intensities for both output waveguides. The experimental data are well fitted by the developed analytical model (Methods), indicating the high robustness of the proposed directional coupler design. The measured maximal transfer of the spin-wave energy takes place at a spin-wave frequency of around 3.48 GHz and is equal to 93.8%, which is only slightly below the theoretical value of 100%. This difference is likely due to imperfections in the fabricated structure and might be decreased by further improvement of the nanostructuring process<sup>37</sup>.

It should be emphasized that complex magnonic circuits are only possible using single-mode waveguides. In these waveguides, width modes are well separated in energy to prevent elastic intermode scatterings<sup>38</sup>. Parasitic scatterings would introduce an energy loss in the signal-carrying mode and create complex interference patterns due to the simultaneous presence of waves with different wavevectors. This is especially critical for concepts based on directional couplers, because different wavevectors also possess different coupling lengths. The waveguides used in our studies are single-mode due to their nanoscopic size, which ensures separation of the modes (Fig. 1b). An additional advantage of the nanoscopic waveguides is spin-wave propagation in longitudinally self-magnetized waveguides, which allows for the efficient two-dimensional (2D) guiding of information<sup>19</sup>.

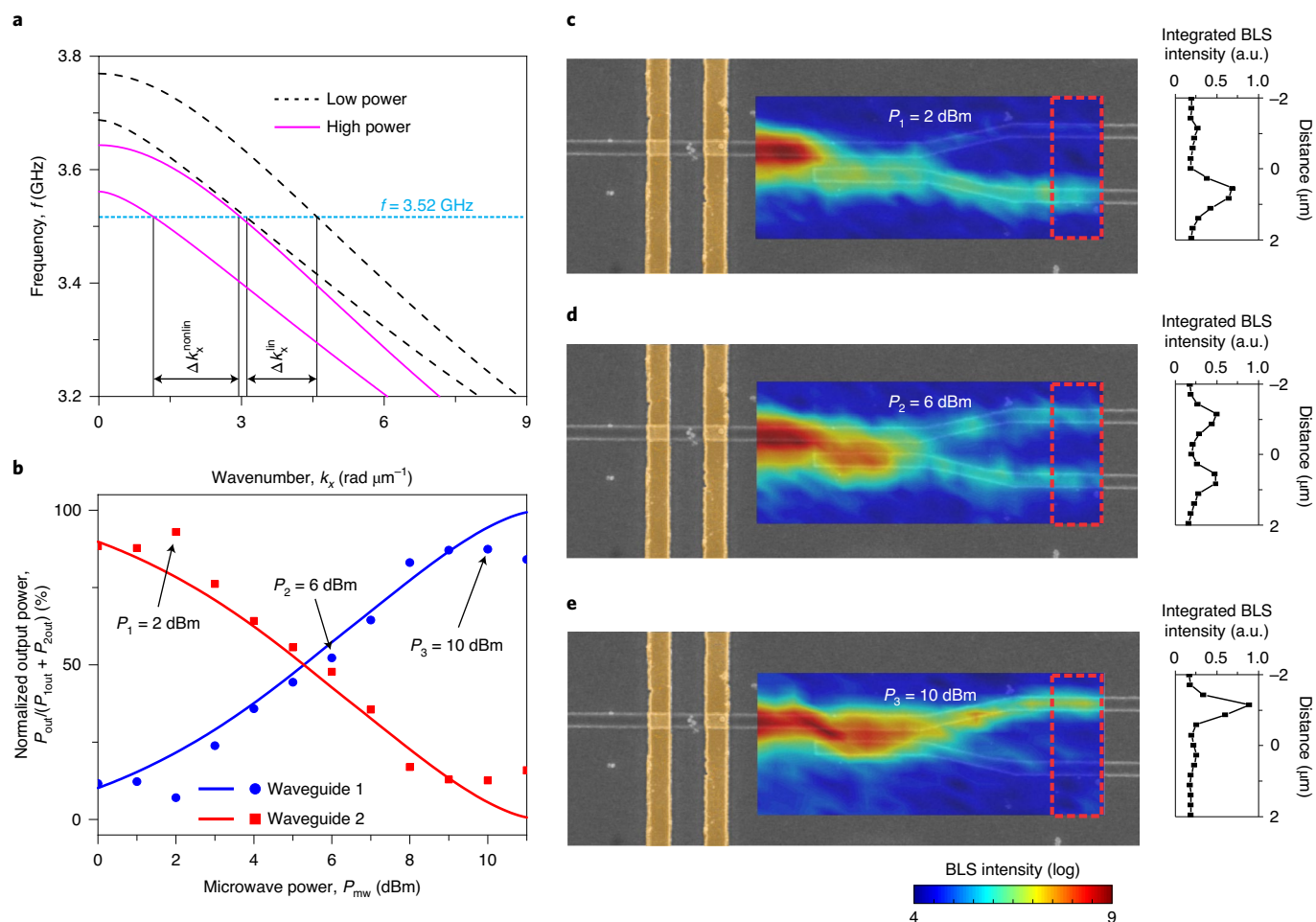


**Fig. 2 | Nonlinear functionality of the directional coupler.** **a**, The dispersion relations of symmetric and antisymmetric spin-wave modes in the coupled waveguides for small (black dashed lines) and large (magenta solid lines) powers. The increase in spin-wave amplitude results in a downshift of the dispersion curves. **b**, Averaged output spin-wave intensity as a function of microwave power  $P_{mw}$  (dots, experimental results; lines, theoretical fits). **c–e**, 2D BLS maps of the spin-wave intensity for a frequency of  $f = 3.52$  GHz and different input powers  $P_1 = 2$  dBm (**c**),  $P_2 = 6$  dBm (**d**) and  $P_3 = 10$  dBm (**e**). The right panels show the spin-wave intensity integrated over the regions indicated by red dashed rectangles.

Two-dimensional BLS spectroscopy scans of the spin-wave intensity are presented in Fig. 1e–g to demonstrate directly the frequency-dependent functionality of the directional coupler. Figure 1e shows the case where most of the spin-wave energy is transferred to the second waveguide at a spin-wave frequency of 3.465 GHz. This planar 2D directional coupler can thus be used to efficiently connect two magnonic conduits without the need for complex and costly 3D bridges, as used in modern electronic circuits. Figure 1g shows an entirely different spin-wave path in the directional coupler. The increase in the spin-wave frequency to  $f_3 = 3.58$  GHz results in a decrease of the coupling length  $L$  by a factor of approximately two. As a result, the spin wave transfers all its energy from the first waveguide to the second one and back. Thus, 86% of the total output spin-wave energy is guided back into the first output waveguide of the directional coupler. This demonstrates the potential use of the directional coupler as a frequency division demultiplexer: if different frequencies are applied to the same input of the directional coupler, they will be transferred to the different outputs of the device. Finally, Fig. 1f demonstrates that the directional coupler can also be used as a 50/50 power splitter, in which half of the spin-wave energy is transferred to the second waveguide and half of it remains in the first one. Such a splitter can also be used as a fan-out logic gate if an amplifier<sup>39–41</sup> is installed at the outputs of the device to

compensate the split in energy. Furthermore, for a fixed frequency, the output signal of the directional coupler can be switched from one output to the other by changing the external field in a small range of  $\Delta B_{ext} = 4.7$  mT (Extended Data Fig. 3 and Supplementary Note 3). Thus, magnetic fields from switchable nanosized magnets<sup>42</sup> could be used to realize a non-volatile nanosecond-fast reconfigurability of the directional coupler.

### Nonlinear switching functionality

The processing of data, in general, requires the utilization of elements with nonlinear characteristics, as provided, for example, by a semiconductor transistor in CMOS. As mentioned above, the key benefits of spin waves for data processing are their pronounced natural nonlinearity, which allows for all-magnon control of one magnonic unit by another. In our studies, the phenomenon of a nonlinear shift of the dispersion relation<sup>9,10</sup> is used, in contrast to the multi-magnon scattering exploited in the realization of a magnon transistor<sup>8</sup>. In the relatively weak nonlinear regime, where the dipolar coupling between the waveguides is larger than the nonlinear frequency shift of the spin waves, nonlinear operation of the directional coupler can be described simply by taking into account the nonlinear frequency shift of the symmetric and antisymmetric collective modes. The shift is the same for both modes and can be well approximated

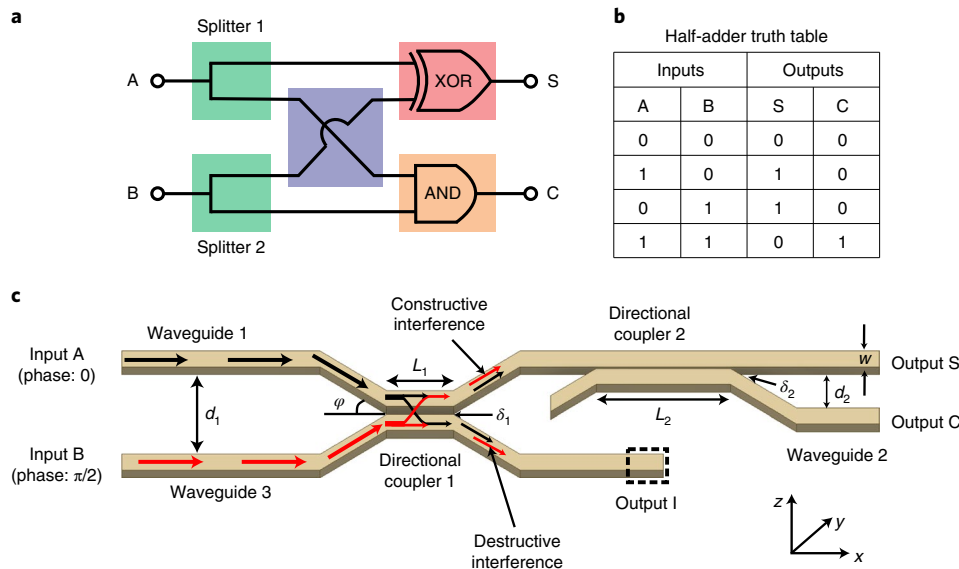


**Fig. 3 | The operational principle of the magnonic half-adder.** **a**, Sketch of the half-adder in electronics format. Building blocks are highlighted by different colours. **b**, Half-adder truth table. **c**, Schematic view of the magnonic half-adder. In this work we consider the following parameters: YIG waveguide width,  $w = 100$  nm; thickness,  $h = 30$  nm; edge-to-edge distances between waveguides,  $d_1 = 450$  nm,  $d_2 = 210$  nm; angle between waveguides,  $\varphi = 20^\circ$ ; gaps between coupled waveguides,  $\delta_1 = 50$  nm,  $\delta_2 = 10$  nm; lengths of coupled waveguides,  $L_1 = 370$  nm and  $L_2 = 3$   $\mu$ m. Red and black arrows show the flow path of magnons from the inputs to the logic gates.

by the nonlinear frequency shift of waves in isolated waveguides<sup>43</sup>:  $f_{s,as}^{(nl)}(k_x, a_k) = f_{s,as}^{(0)}(k_x) + T_k |a_k|^2$ , where  $f_{s,as}^{(0)}(k_x)$  are the dispersion relations of the symmetric and antisymmetric modes of the coupled waveguides in the linear region<sup>19</sup>,  $a_k$  is the canonical spin-wave amplitude and  $T_k$  is the nonlinear shift coefficient (Methods). For the backward volume geometry ( $M_s || k_x$ , where  $M_s$  is the saturation magnetization and  $k_x$  is the wavenumber) used here, the nonlinear shift coefficient is negative<sup>9,43</sup>, so the spin-wave dispersion curves shift down with an increase in the spin-wave amplitude, defined by the applied RF power. The calculated spin-wave dispersions are shown in Fig. 2a for small and large applied microwave powers. As can be seen, for a fixed spin-wave frequency of 3.52 GHz, the coupling length  $L$  decreases from  $\pi/\Delta k_x^{\text{lin}}$  to  $\pi/\Delta k_x^{\text{nonlin}}$  with an increase in input power, resulting in changed device characteristics.

To study the nonlinear switching functionality of the presented directional coupler, the microwave power  $P_{\text{mw}}$  was varied in the range from 0 dBm to 11 dBm. Figure 2b clearly shows that the respective output spin-wave intensity strongly depends on the input microwave power due to the discussed nonlinear effects. Figure 2c shows that, for a relatively low input power 2 dBm, the output spin-wave energy is transferred to the second waveguide. This regime can be considered a linear one. For an increased power of 6 dBm, the spin-wave dispersion shift implies that half of the output spin-wave energy is transferred back to the first waveguide and thus the directional coupler; accordingly, it works as a 50/50 splitter. A further increase of the input power to 10 dBm results in a further dispersion shift, a decrease of the coupling length  $L$  and a transfer of the spin-wave energy back to the first waveguide, as can be seen in Fig. 2e.

### Design of the all-magnon half-adder

According to the obtained experimental results, we propose an integrated magnonic circuit on the example of a half-adder consisting of two directional couplers and investigate its functionality by means of micromagnetic simulations. The simulations allow us to check the working principle of this design at a size comparable to a CMOS device and also to perform benchmarking. For the simulations, we chose a minimal waveguide width of 100 nm (see Fig. 3 for the sizes

of the structure), which can be reliably fabricated using modern patterning techniques<sup>4,15,37,44</sup> (Methods).

A general schematic layout of a half-adder, in electronics form, is presented in Fig. 3a. This combines an XOR logic gate and an AND logic gate using 3D bridge constructions. It adds two single binary digital inputs 'A' and 'B' and has two outputs, sum ('S') and carry ('C'). The truth table of a half-adder is shown in Fig. 3b and a sketch of the proposed magnonic half-adder is presented in Fig. 3c. Directional coupler 1 in the magnonic half-adder acts as a power splitter for each of the two inputs and, at the same time, replaces the 3D bridge required for sending the signals from input A to the AND gate and from input B to the XOR gate (compare Fig. 3a). The spin-wave flow paths in the magnonic half-adder are shown by the black and red arrows in Fig. 3c: spin waves from both inputs are split into two identical spin waves of half intensity by directional coupler 1. One pair of waves is directed to directional coupler 2 via waveguide 1 and the other pair is guided into the idle output 'I' via waveguide 3. In the present simulation, output 'I' just features a high damping region at the end (shown in the figure by a dashed rectangle) and it does not contribute to the half-adding function. However, it acts as an XOR logic gate and, with the use of another directional coupler, can perform the same half-adder operation (Extended Data Fig. 4 and Supplementary Note 4). Thus, the modified half-adder can be considered as a combination of a half-adder with a fan-out logic gate, which doubles each output of the device. Directional coupler 2 performs the actual half-adder logic operation and its operational principle is described in the next section.

### Modelling of the nonlinear functionality

The nonlinear functionality of the directional coupler shown above qualitatively takes place for any spin-wave directional coupler. Nevertheless, as shown below, realization of the logic operation requires a full switch of the spin-wave path by the change in the spin-wave intensity exactly four times. To achieve this value, modifications of the directional coupler, discussed below, are required.

Directional coupler 2 consists of a coupled straight parallel waveguide with 3- $\mu$ m coupled length as shown in Fig. 4a. The split

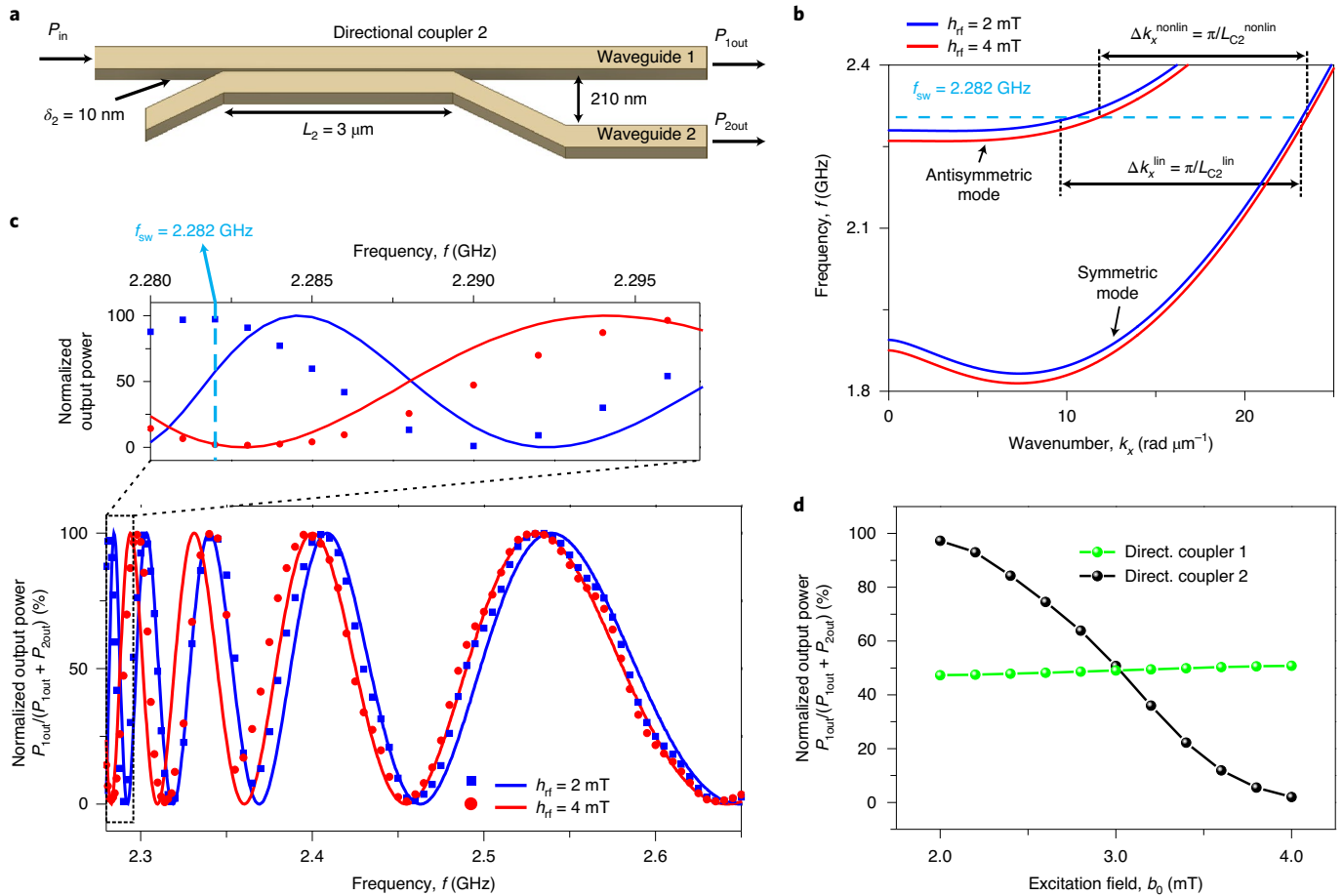


**Fig. 4 | Modelling and characteristics of directional coupler 2.** **a**, Schematic of directional coupler 2. **b**, Analytically calculated dispersion curves for the coupled waveguides for small (blue lines) and large (red lines) excitation fields  $h_{rf}$ . The change in coupling length  $L_{C2}$  is clearly visible, and is associated with the increase in spin-wave amplitude. **c**, Normalized output power in the first waveguide  $P_{1out}/(P_{1out} + P_{2out})$  as a function of frequency for different excitation field  $h_{rf}$  (symbols, simulations; lines, analytic theory). An enlarged view of the region marked with the dashed rectangle is shown in the top panel. **d**, Simulated normalized output power  $P_{1out}$  as a function of excitation field  $b_0$  for a fixed frequency of  $f = 2.282$  GHz for directional couplers 1 and 2.

dispersion relations in the linear regime in the coupled waveguides are shown in Fig. 4b as blue lines. To obtain the linear dispersion, small spin-wave amplitudes are excited by a microwave field of  $h_{rf} = 2$  mT. The output power in the first waveguide normalized by the total power  $P_{1out}/(P_{1out} + P_{2out})$  can be expressed using the characteristic coupling length  $L_{C2}$ :  $\frac{P_{1out}}{P_{1out} + P_{2out}} = \cos^2(\pi L_2 / (2L_{C2}))$ , where  $L_2 = 3 \mu\text{m}$  is the length of the coupled waveguide in directional coupler 2. Figure 4c shows the normalized output power in the first waveguide as a function of spin-wave frequency  $f$ , in the frequency range from 2.28 GHz to 2.65 GHz. The result of numerical simulations in the linear regime is shown with blue symbols and the analytic calculation with solid blue lines. One can clearly see that the output power  $P_{1out}$  strongly depends on the spin-wave frequency, as shown experimentally in Fig. 2. This is due to the strong dependence of the coupling length  $L_{C2}$  on the spin-wave wavenumber<sup>19,35,45</sup>. The coupling length consequently defines the energy distribution between the output waveguides for a given length of the coupled waveguides. The small mismatch between simulations and theory in the region below 2.3 GHz is mainly caused by the damping, which is not taken into account in the theory, and by the large sensitivity of the coupling coefficient to the dispersion of the anti-symmetric mode, which is practically flat in this region.

When the input spin-wave power increases, spin-wave dispersion shifts down (red lines in Fig. 4b). Thus, for a fixed spin-wave frequency of 2.282 GHz, the wavenumber difference  $\Delta k_x = \pi/L_{C2}$

changes from  $\Delta k_x^{\text{lin}}$  to  $\Delta k_x^{\text{nonlin}}$  with an increase in the excitation field from  $b_0 = 2$  mT to 4 mT. Consequently, the coupling length  $L_{C2}$  of the directional coupler also changes. Using the Taylor expansion of the frequency dependence of the coupling length, the power dependence of the output of directional coupler 2 can be found:

$$\frac{P_{1out}}{P_{1out} + P_{2out}} = \cos^2\left(\frac{\pi L_2}{2L_{C2}^{\text{lin}}} - \frac{L_2}{L_{C2}^{\text{lin}}} \frac{\pi}{2L_{C2}^{\text{lin}}} \frac{\partial L_{C2}}{\partial f} T_k |a_k|^2\right) \quad (1)$$

The power-independent term is proportional to the ratio of the directional coupler length to the coupling length in the linear regime  $L_2/L_{C2}^{\text{lin}}$ . The output power  $P_{1out}$  periodically changes with a change in the coupling length and is maximal for the cases  $L_2/L_{C2}^{\text{lin}} = 0, 2, 4, \dots$  (Fig. 4c). Simultaneously, as seen from equation (1), the sensitivity to the nonlinear effect increases with an increase in the ratio  $L_2/L_{C2}^{\text{lin}}$ . Therefore, the longer the directional coupler is and the more coupling lengths it spans, the higher the nonlinear phase accumulation. This is the reason why directional coupler 2 in our half-adder design is long and features a strong coupling provided by the small gap between the waveguides of only 10 nm. It has a length of  $L_2 = 14L_{C2}^{\text{lin}}$  and is very sensitive to the increase in the spin-wave amplitude passing through it. As a result, a complete energy transfer from output 1 to output 2 is observed in the micromagnetic simulations if the spin-wave intensity is increased by a factor of four ( $L_2 = 13L_{C2}^{\text{nonlin}}$ , black line in Fig. 4d). The normalized

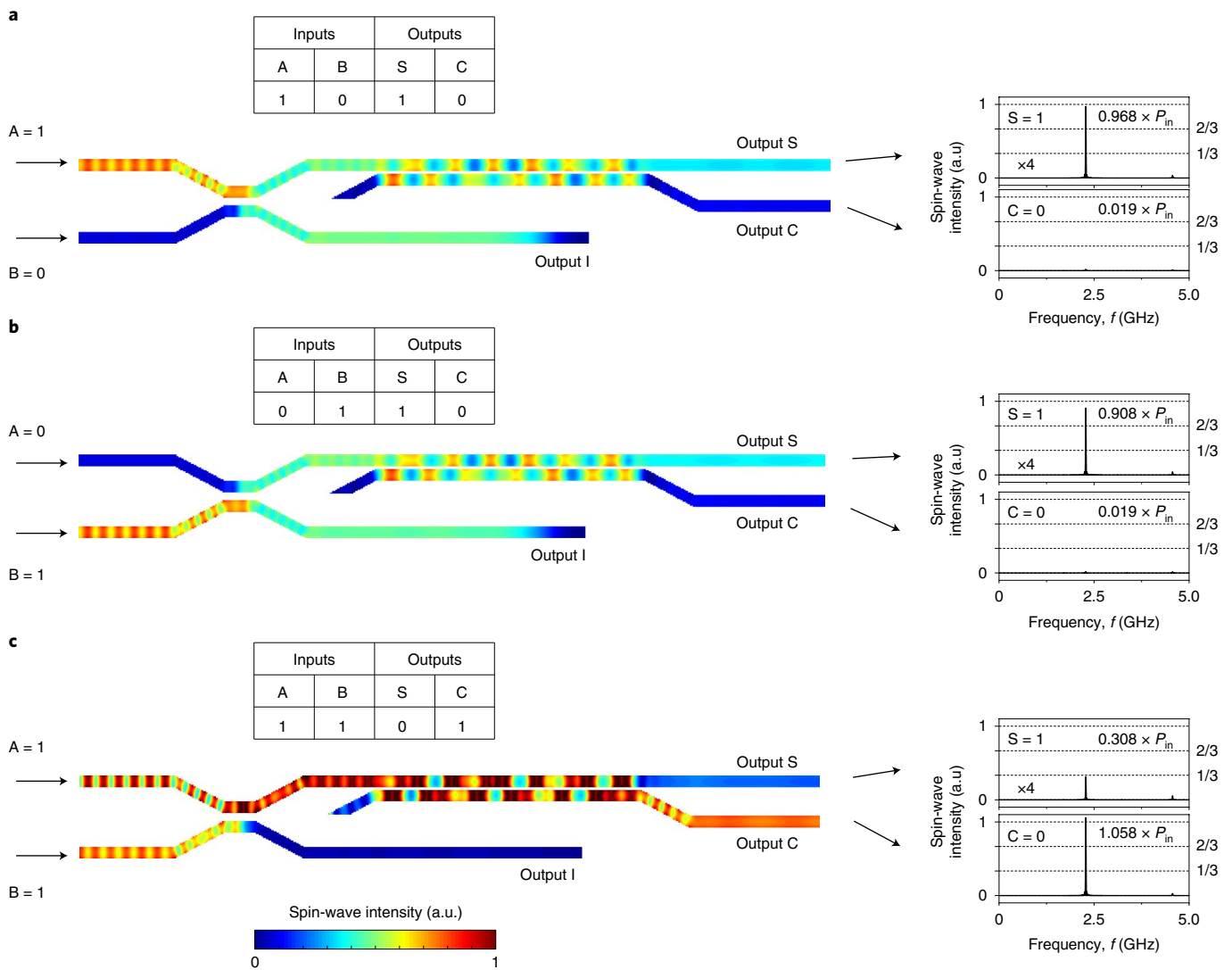


**Fig. 5 | Operational principle of the magnonic half-adder. a–c,** Spin-wave intensity distributions for different inputs combinations: A = 1, B = 0 (**a**), A = 0, B = 1 (**b**) and A = 1, B = 1 (**c**). The truth tables for each input combination are shown above the structures. The normalized output spin-wave intensities in the outputs are shown on the right. All outputs S are multiplied by a factor of four.

output spin-wave power in the first waveguide decreases from 97.3% at  $b_0 = 2$  mT to 2.0% at  $b_0 = 4$  mT. Owing to this nonlinear switching effect, directional coupler 2 performs a combined AND and XOR logic function, as will be described in the following. At the same time, the first directional coupler 1 in the half-adder design should remain in the linear regime and its coupling length should be independent of the spin-wave power. This is achieved by its smaller length of 370 nm as well as via an increased spacing between the waveguides of 50 nm. As a result, directional coupler 1 spans only half of the coupling length  $L_1 = 0.5L_{C1}^{lin}$ , independent of the excitation field (green symbols in Fig. 4d). The directional coupler studied experimentally above was designed for linear functionality. Nevertheless, the increase of the spin-wave power from 0 dBm to 10 dBm, which is a more than four times increase of the spin-wave intensity required by the half-adder design, also results in the nonlinear switch (Fig. 2).

### Operational principle of the magnonic half-adder

The operational principle of the half-adder is shown in Fig. 5. Binary data are coded into the spin-wave amplitude; namely, in the ideal case, a spin wave of a given amplitude (for example,  $M_z/M_s = 0.057$ , where

$M_z$  is the out-of-plane ( $z$ ) component of dynamic magnetization) corresponds to logic state ‘1’, while zero spin-wave amplitude corresponds to ‘0’. In the following, we normalize output spin-wave intensity to the input spin-wave intensity. In the more realistic cases considered below, we utilize an approach from CMOS: a normalized spin-wave intensity below 1/3 is considered to be logic ‘0’ and above 2/3, logic ‘1’.

The operational principle of the half-adder is as follows. Let us first consider the case of logic inputs A = 1 and B = 0 (Fig. 5a). In this case, the spin wave injected into input A is split into two equal parts by directional coupler 1. One part is directly guided to directional coupler 2 by the upper conduit. The spin-wave intensity is chosen in such a way that directional coupler 2 remains in the linear regime ( $L_{C2}^{lin} \approx 214$  nm  $\approx 14/L_2$ ) and, after initial oscillations, the spin wave is guided into output S, as shown in Fig. 5a. Only about 1.9% of the spin-wave energy goes into output C. This corresponds to logic outputs S = 1 and C = 0. If a spin wave is injected in input B only, this corresponds to logic inputs A = 0 and B = 1 (Fig. 5b). The situation in this case is quite similar to the previous one. The situation is different for input logics states A = 1 and B = 1 (Fig. 5c). It is assumed that the phase of the spin wave injected into input

B is permanently shifted by  $\pi/2$  with respect to the one in input A (to compensate the  $-\pi/2$  phase shift caused by directional coupler 1), which can be easily realized by many means<sup>46</sup>. In this case, constructive interference of the two spin waves will take place in waveguide 1 and destructive interference in waveguide 3. As a result of this coherent superposition, the entire spin-wave energy from both inputs goes to directional coupler 2, resulting in four times larger spin-wave intensity with respect to the single-input cases when only 50% of the spin-wave energy is guided to this coupler. As discussed above, this increase in spin-wave intensity by a factor of four switches the coupler to the nonlinear regime ( $L_{C_2}^{\text{nonlin}} \approx 230 \text{ nm} \approx 13/L_2$ ) and the spin wave is guided to output C. This corresponds to logic outputs  $S=0$  and  $C=1$  (Fig. 5c) and, thus, the whole truth table of the half-adder is realized.

Note that the all-magnon circuit concept<sup>8,34</sup> requires that the signal from the output of a magnonics gate be directly guided into the input of the next one. To satisfy this condition, the spin-wave intensity at outputs S still has to be amplified by a factor of approximately four due to the energy splitting in directional coupler 1 and also parasitic reflections and spin-wave damping in the waveguides. The output signals S shown in Fig. 5 are artificially multiplied by four. The most promising realization of such an amplifier is based on the utilization of voltage-controlled magnetic anisotropy (VCMA) parametric pumping<sup>43,47,48</sup> (Extended Data Fig. 5 and Supplementary Note 5). By contrast, no amplifier is required for the ‘carry’ output of the half-adder. In general, the idea presented here and the concept of the half-adder are applicable to any magnetic material. Nevertheless, the requirement that the device length  $L_{\text{dc}}$  be smaller than the spin-wave decay length should be satisfied. This is the case not only for YIG, but also for low-damping Heusler compounds<sup>49</sup>.

### Benchmarking of the proposed technology

A summary of the key parameters of two versions of the proposed half-adder is provided in Table 1 (Methods): the first one is the device that was simulated and discussed above. The second device is an estimation performed for a device with  $w=30 \text{ nm}$ ,  $h=10 \text{ nm}$  and minimal gap  $\delta=10 \text{ nm}$ . It has to be mentioned that the second device does not constitute a fundamental limit but is merely an estimation based on the current state of the art of fabrication technology<sup>15,37</sup>. A further improvement in all characteristics is potentially achievable.

According to Table 1, the area of the simulated 100-nm-feature-size half-adder is  $5.58 \mu\text{m}^2$  (the spaces between neighbouring logic gates are included) and is thus only a few times larger than a corresponding 7-nm-feature-size CMOS device. In contrast to a CMOS realization, the magnonic half-adder core part (without amplifier) consists of only three nanowires made of the material and of only one planar layer. This drastically simplifies its fabrication and decreases its potential costs. The area can be readily decreased to  $1.016 \mu\text{m}^2$  for the second 30-nm-based device, which is comparable to the 7-nm-based CMOS device. In addition, it should be noted that the largest part of the half-adder is provided by directional coupler 2; this could be further decreased by utilizing exchange-coupling mechanisms between the waveguides instead of dipolar coupling. To achieve this, the air gap between the coupled waveguides should be filled with another magnetic material.

Operational frequency is an important requirement. In the presented half-adder, the delay time is defined by the whole length of the device with respect to the spin-wave group velocity. In our design, the spin-wave propagation time from input to output is  $\sim 150 \text{ ns}$ . According to Table 1, the calculation time can be reduced to 18 ns in the second device. This value is larger than the 60-ps delay time obtained for 7-nm CMOS and suggests that magnon logic would be more suitable for slow but low-energy applications. At the same time, one has to note that CMOS does not operate at its maximal speed because of the drastically increasing Joule heating (a typical clock rate is 3 GHz, which corresponds to  $\sim 0.3\text{-ns}$  delay).

**Table 1 | Magnonic half-adder benchmarking**

| Parameters   | YIG <sup>a</sup><br>(100 nm) | YIG <sup>b</sup> (30 nm) | CMOS <sup>c</sup><br>(7 nm) |
|--|------------------------------|--------------------------|-----------------------------|
| Area ( $\mu\text{m}^2$ )   | 5.58                         | 1.016                    | 1.024                       |
| Delay time (ns)  | 150                          | 18                       | $6 \times 10^{-2}$          |
| Total energy consumption without amplification (aJ)                        | 24.6                         | 1.96                     | 35.3                        |
| Spin-wave frequency (GHz)  | 2.282                        | 2.39                     | -                           |
| Spin-wave wavelength (nm)  | 340                          | 510                      | -                           |
| Spin-wave group velocity ( $\text{m s}^{-1}$ )                             | 25                           | 137                      | -                           |
| <b>Type of amplifier</b>   | <b>Energy consumption</b>    |                          |                             |
| Electric current-based parametric pumping <sup>39,41</sup>                 | $10^5$ (aJ per operation)    |                          |                             |
| Voltage-controlled magnetic anisotropy parametric pumping <sup>43,47</sup> | 3 (aJ per operation)         |                          |                             |

<sup>a</sup>The values in this column are extracted from the micromagnetic simulation of the half-adder investigated in this Article. <sup>b</sup>The values are estimated characteristics of a device miniaturized down to 30 nm using equations (8) to (10) (Methods). <sup>c</sup>The values are calculated using Cadence Genus by Sorin D. Cotofana for 7-nm CMOS technology.

In computing systems, small energy consumption is probably the most crucial requirement, given the constantly increasing amount of information that has to be processed. In our simulations, we recorded the total energy of the device as a function of simulation time. The energy injected into the device per nanosecond is equal to  $4.1 \times 10^{-20} \text{ J ns}^{-1}$  for the input combinations  $A=1$  and  $B=1$ . Note that only the energy propagating along the positive direction is taken into account. For the 300-ns pulse duration the energy consumption is thus 12.3 aJ. For all operations, the total energy consumption is 24.6 aJ. This is similar to current CMOS values (35.3 aJ), calculated using Cadence Genus (Methods). It should be highlighted that the energy consumption of the miniaturized 30-nm-based device is more than one order of magnitude smaller ( $\sim 1.96$  aJ). At the same time, we have to underline that this energy consumption is related to the energy within the magnonic domain only and the energy consumption of the amplifier should be added (Table 1 and Supplementary Note 5). The most promising approach is VCMA parametric pumping, which has been reported recently<sup>43,47,48</sup> and allows for an energy consumption of an amplifier of  $\sim 3$  aJ per device.

### Conclusions

We have fabricated a submicrometre spin-wave directional coupler operating in a single-mode regime and studied its functionality in the linear and nonlinear regime using  $\mu\text{BLS}$  spectroscopy. Our experimental results are supported by numerical simulations and analytical theory. By varying the applied microwave frequency or an applied magnetic field, spin waves can be guided to different coupler outputs, demonstrating the reconfigurability of the device. Our spin-wave directional coupler could therefore be used as a microwave filter for processing analogue and digital information, a power splitter for fan-out logic gates, a frequency divider or signal multiplexer, and a planar interconnecting element for magnonic conduits. Furthermore, the output of the directional coupler can be switched by changing the spin-wave amplitude, demonstrating nonlinear functionality.

We have also proposed and tested numerically an integrated magnonic circuit—a half-adder—based on the fabricated directional

coupler. This half-adder consists of two directional couplers: one that functions as a linear power splitter and one that functions as a nonlinear switch (as demonstrated experimentally). The proposed device is all-magnonic—the magnons are controlled by magnons without any conversion to the electric domain—ensuring low energy consumption. The proposed magnonic half-adder consists only of three planar magnetic nanowires with one amplifier and can potentially substitute 14 transistors in electronics circuits. A magnonic half-adder developed with 30-nm technology is predicted to have a footprint comparable to a 7-nm CMOS half-adder, with around 10 times smaller energy consumption.

## Methods

**Liquid-phase epitaxial film growth and sample fabrication.** An 85-nm-thick YIG film was grown on a 1-inch (111) 500- $\mu\text{m}$ -thick gadolinium gallium garnet (GGG) substrate by liquid-phase epitaxy from PbO-B<sub>2</sub>O<sub>3</sub>-based high-temperature solutions at 860 °C using the isothermal dipping method (for example, ref. <sup>50</sup>). Nominally pure Y<sub>3</sub>Fe<sub>5</sub>O<sub>12</sub> films with smooth surfaces were obtained on horizontally rotated substrates applying rotation rates of 100 r.p.m. (refs. <sup>67</sup>). The saturation magnetization of the YIG film is  $1.42 \times 10^5 \text{ A m}^{-1}$  and its Gilbert damping  $\alpha = 2.1 \times 10^{-4}$ , as extracted by ferromagnetic resonance spectroscopy<sup>51</sup>.

The directional coupler was fabricated using electron-beam lithography, Ar<sup>+</sup> ion-beam etching and electron-beam evaporation. First a double layer of polymethyl methacrylate was spin-coated on the YIG film and the directional coupler structures were created afterwards by electron-beam lithography. To obtain well-shaped waveguides, titanium and chromium were deposited by electron-beam evaporation as a bilayer hard mask, defining the shape of the directional coupler structures. These were then etched out of the film by Ar<sup>+</sup> ion-beam etching. Finally, the U-shaped antenna was defined by electron-beam lithography and a liftoff process. This consisted of ~230-nm-thick gold and 20-nm-thick titanium (for adhesion).

**BLS spectroscopy and spin-wave excitation.**  $\mu\text{BLS}$  spectroscopy is a technique for the measurements of spin-wave intensities with frequency, space, phase and time resolution<sup>36</sup>. It is based on inelastic light scattering of the incident laser beam by magnons. In our measurements, a laser beam of 491-nm wavelength and power of 1.8 mW was focused on the directional coupler with an effective spot diameter of 400 nm using a  $\times 100$  microscope objective with a large numerical aperture (NA = 0.75). The scattered light was collected and guided into a tandem Fabry-Pérot interferometer (TFP-1, JRS Scientific Instruments) for further analysis. To perform 2D scans, the sample was moved with respect to the laser spot in steps of a few hundred nanometres in each direction using a piezoelectric stage. Stabilization marks were grown on the sample to maintain the same relative position of the laser spot during the long measuring cycles.

An external magnetic field,  $B_{\text{ext}} = 56 \text{ mT}$ , was applied along the YIG conduits ( $x$  axis) to saturate the directional coupler in a backward volume geometry<sup>34</sup>, and a RF current with power  $P_{\text{mw}} = 0 \text{ dBm}$  (in the linear regime) was applied to the antenna to excite spin waves. Spin-wave frequencies ranging from 3.4 GHz to 3.63 GHz were excited well by the U-shaped antenna in the isolated waveguide (Extended Data Fig. 2 and Supplementary Note 2). Only the first width mode was excited in this frequency range, as shown in the dispersion curve in Fig. 1b.

**Calculation of the nonlinear frequency shift coefficient.** The nonlinear shift coefficient  $T_k$  in the isolated waveguide can be calculated using the framework of ref. <sup>9</sup> and by assuming a uniform mode profile across the waveguide thickness and width. Accounting for the negligible static demagnetization of a waveguide along its length,  $F_0^{\text{xx}} = 0$ , the nonlinear shift coefficient becomes equal to<sup>40</sup>

$$T_k = \left( (\omega_{\text{H}} - A_k) + \frac{B_k^2}{2\omega_0^2} (\omega_{\text{M}} (4\lambda^2 k_x^2 + F_{2k}^{\text{xx}}(0)) + 3\omega_{\text{H}}) \right) / 2\pi \quad (2)$$

where

$$A_k = \omega_{\text{H}} + \frac{\omega_{\text{M}}}{2} (2\lambda^2 k_x^2 + F_k^{\text{yy}}(0) + F_k^{\text{zz}}(0)) \quad (3)$$

$$B_k = \frac{\omega_{\text{M}}}{2} (F_k^{\text{yy}}(0) - F_k^{\text{zz}}(0)) \quad (4)$$

The relation between the dynamic magnetization component and the canonical spin-wave amplitude  $a_k$  is given by

$$M_z = M_s a_k \sqrt{2 - |a_k|^2} (u_k - v_k) \quad (5)$$

with

$$u_k = \sqrt{\frac{A_k + \omega_0}{2\omega_0}} \text{ and } v_k = -\text{sign}[B_k] \sqrt{\frac{A_k - \omega_0}{2\omega_0}} \quad (6)$$

**Calculation of the directional coupler characteristics.** The theory of the directional coupler is described in our previous paper<sup>19</sup>. However, in ref. <sup>19</sup> we accounted only for the straight part of the coupler where the distance between waveguides is minimal and constant. For the device reported in this Article, this approach is not sufficient, because the gap between the coupled waveguides is quite large (320 nm). In such a case, the region of the bent waveguides could also notably contribute to the coupling characteristics, because the gap in this region is not much larger than the minimal gap over a considerable distance. To take this bent region into account, we calculated the splitting of the symmetric and antisymmetric spin-wave modes as a function of the gap,  $\Delta k = \Delta k(d)$ . The coordinate dependence of the spin-wave power in the waveguides is then given by

$$\begin{aligned} P_1(x) &= \cos^2 \left[ \frac{1}{2} \int_0^x \Delta k(d(x')) dx' \right] \\ P_2(x) &= \sin^2 \left[ \frac{1}{2} \int_0^x \Delta k(d(x')) dx' \right] \end{aligned} \quad (7)$$

Furthermore, an additional coupling, which is especially pronounced for large spin-wave wavelengths, must be taken into account due to the large wavelength studied in this work: the part of the first waveguide located before the second one starts also contributes to the coupling 'diagonally'. Indeed, the dynamic magnetization of a large spin-wave wavelength varies slowly and, thus, the mentioned part of the first waveguide creates a non-negligible dipolar field at the beginning of the second one. By contrast, for short-wavelength spin waves, these additional contributions vanish, because contributions from neighbouring half-wavelength parts almost cancel each other. In this work, we account for it through the introduction of an 'additional effective length' of the coupler, which, by itself, depends on the spin-wave wavelength. Because the strength of the dipolar fields decays with the distance approximately proportional to  $x^{-3}$ , the effective length is expected to depend on spin-wave wavenumber as  $L_{\text{eff}} = C_1 / (k + C_2)^2$ . Here, the second power in the spin-wave wavenumber comes from the integration  $\int_0^{1/k} (x + d_0)^{-3} dx$ , and the constant  $C_2$  reflects the fact that the effective length cannot increase infinitely for an infinitely large spin-wave wavelength. By fitting the experimental data, we found  $C_1 = 25 \mu\text{m}^{-1}$  and  $C_2 = 2 \mu\text{m}^{-1}$ . Using this expression for the effective additional length, both frequency and field dependencies of the power transmission rates are described well (Figs. 1d and 2b).

The variation of the power transmission rate in the coupler with increasing spin-wave power is mainly attributed to the nonlinear frequency shift of the symmetric and antisymmetric spin-wave modes in coupled waveguides, as shown in Fig. 3b. The shift of the dispersion results in a change of spin-wave wavenumbers at a given frequency and, consequently, in a change of the coupling between the waveguides. Knowing the frequency dependence of the power transmission rates  $P_{1,2}^{(\text{lin})}(\omega)$  in the linear regime, the nonlinear characteristics can be calculated simply as  $P_{1,2}^{(\text{nl})}(\omega, a) = P_{1,2}^{(\text{lin})}(\omega - T_k |a|^2)$ , where  $a$  is the canonical spin-wave amplitude and  $T_k$  is the nonlinear frequency shift ( $T_k / 2\pi = -1.8 \text{ GHz}$  in our case). Given that the experimental data measured for 0-dBm excitation power also correspond to a weakly nonlinear regime, for the description of power dependence we use the relation  $P_{1,2}^{(\text{nl})}(\omega, a) = P_{1,2}^{(0)}(\omega - T_k (|a|^2 - |a_0|^2))$ , where  $P_{1,2}^{(0)}$  is the dependence for 0 dBm (measured and fitted by the calculations shown above) and  $a_0$  is the spin-wave amplitude at 0-dBm excitation power. The relation of the spin-wave amplitude with the excitation power was obtained by measuring the BLS intensity in the first waveguide before the coupler and fitting one adjusting parameter (the ratio of BLS counts to the square of the spin-wave amplitude). We get the following relation  $a = 0.035 \sqrt{1 + p/17.4}$ , where  $p$  is the excitation power in dBm. The appearance of an almost linear dependence of the spin wave power on  $p$ , instead of an exponential one, which could be expected, is mediated by the strong variation of the spin-wave group velocity with spin-wave wavenumber and, consequently, with the excitation power at a given frequency. The described simple model fits the experimental data well for the applied powers below 10 dBm (Fig. 3a). For higher powers, higher-order nonlinear effects should be taken into account as well<sup>32</sup>.

**Micromagnetic simulations.** Dispersion curve presented in Fig. 1b. The micromagnetic simulations were performed by the GPU-accelerated simulation program Mumax3 to calculate the space- and time-dependent magnetization dynamics in the investigated structures using a finite-difference discretization<sup>33</sup>. The following material parameters were used: saturation magnetization  $M_s = 1.33 \times 10^5 \text{ A m}^{-1}$  (94% comparing to the value of the plain film<sup>67</sup> due to the Ar<sup>+</sup> ion-beam etching) and Gilbert damping  $\alpha = 2 \times 10^{-4}$ . A standard exchange constant for YIG of  $A = 3.5 \text{ pJ m}^{-1}$  was assumed. There were three steps involved in calculation of the spin-wave dispersion curve<sup>34</sup>: (1) the external field was applied along the waveguide and the magnetization was relaxed to a stationary state (ground state); (2) a sinc field pulse  $b_y = b_0 \text{sinc}(2\pi f t)$ , with an oscillation field of  $b_0 = 1 \text{ mT}$  and a cutoff frequency of  $f_c = 10 \text{ GHz}$ , was used to excite a wide range of spin waves; (3) the spin-wave dispersion relations were obtained by performing 2D fast Fourier transformation (FFT) of the time- and space-dependent data.

**Magnonic half-adder.** The simulated structure of the magnonic half-adder is shown in Fig. 1c. The parameters of the nanometre-thick YIG were obtained from experiments and are as follows<sup>67</sup>: saturation magnetization  $M_s = 1.4 \times 10^5 \text{ A m}^{-1}$ , exchange constant  $A = 3.5 \text{ pJ m}^{-1}$  and Gilbert damping  $\alpha = 2 \times 10^{-4}$ . The damping at the ends of the simulated structure and the high damping absorber was set to exponentially increase to 0.5 to prevent spin-wave reflection<sup>55</sup>. The high damping

region could be realized in the experiment by putting another magnetic material or metal on top of the YIG to enhance the damping or it can just correspond to waves guided into further parts of the magnonic network. No external bias field was applied. The static magnetization oriented itself parallel to the waveguides spontaneously due to the strong shape anisotropy in the nanoscale waveguides. The mesh was set to  $10 \times 10 \times 30 \text{ nm}^3$ . To excite propagating spin waves, a sinusoidal magnetic field  $b = b_0 \sin(2\pi ft)$  was applied over an area of 100 nm in length, with a varying oscillation amplitude  $b_0$  and microwave frequency  $f$ .  $M_z(x, y, t)$  of each cell was collected over a period of 300 ns, which is long enough to reach the steady state. The fluctuations  $m_z(x, y, t)$  were calculated for all cells via  $m_z(x, y, t) = M_z(x, y, t) - M_z(x, y, 0)$ , where  $M_z(x, y, 0)$  corresponds to the ground state. The spin-wave spectra of the output signals were calculated by performing a fast Fourier transformation from 250 ns to 300 ns, which corresponds to the steady state. We mention that all these simulations were performed for defect-free waveguides and without taking temperature into account. The influences of edge roughness, trapezoidal cross-sections of the waveguides and temperature can be ignored due to their smallness, as has been shown in our previous studies<sup>15,19</sup>.

**Energy consumption.** For the estimation of energy consumption in the magnonic system (neglecting transducers), the minimal energy consumption can be expressed as (Supplementary Note 6)

$$E = \frac{20\pi M_s v_{gr} f S}{3 \gamma T_k} \quad (8)$$

where  $v_{gr} = 2\pi \frac{\partial f}{\partial k}$  is the spin-wave group velocity and  $S$  is the cross-section of the waveguide. As one can see, the energy consumption is independent of the characteristics of spin-wave couplers and spin-wave amplitude. Note that the nonlinear frequency shift  $T_k$  is of the order of the spin-wave frequency  $f$  ( $T_k \propto f$ ), especially in the exchange-dominated region. The conclusion is reached that the feasible way to reduce energy consumption is to decrease the waveguide cross-section  $S$ . Another alternative is to search for specific points or mechanisms with anomalously high nonlinearity. It should be noted that the relation of equation (8) is universal and occurs in other realizations of magnonic half-adders that are based on the nonlinear shift. For the other designs, the only change is the pre-factor  $20\pi/3$ .

**Scalability and delay time.** The width of the device can be estimated by

$$w_{de} = 2w + 4 \times 5h \quad (9)$$

where  $w$  is the width of the waveguide and  $h$  is the thickness of the waveguide. This equation accounts for the minimal distance between all waveguides and neighbouring devices of  $5h$  to make the dipolar interaction relatively weak. The gaps between different logic gates are taken into account in this width.

The length of the device is given by

$$L_{de} = (N + 0.5)L_C + 4 \frac{5h}{\sin \varphi} \quad (10)$$

where  $\varphi$  is the angle of the bent waveguide,  $L_C$  is the coupling length and  $N = L_2/L_C$  is the ratio between the coupled length of directional coupler 2 and the coupling length. The minimal  $N$  can be estimated from the condition that directional coupler 1, working at half the coupling length, does not substantially change its characteristics at power that is sufficient to switch directional coupler 2. Simple calculations yield that the change of directional coupler 1 transmission is given by  $\cos^2(\pi(N-1)/(4N))$ , while in the linear regime the transmission rate is equal to 1/2. This gives the restriction  $N_{\min} = 6$ . The area of the magnonic half-adder is equal to  $w_{de}L_{de}$ . The processing delay is  $\tau_d = L_{de}/v_{gr}$ .

**Calculation of the energy consumption of the 7-nm CMOS half-adder.** We considered a 7-nm half-adder standard cell afferent to the typical processor corner (room temperature, 0.7-V power supply) and evaluated its power consumption using Cadence Genus. To this end, we set an inverter standard cell as driver and a capacitance of 2.5 fF as the output load, and assumed for the nets a 50% probability of logic '1' and a toggle rate of 0.02 ps. The simulation results indicate a total power consumption of 587.994 nW, of which the dynamic component (divided into nets' power and internal power, which account for 87.7% and 13.3% of the dynamic power, respectively) dominates the less than 1-nW leakage component.

## Data availability

The data that support the plots within this paper and other findings of this study are available from the corresponding author upon reasonable request.

Received: 7 February 2019; Accepted: 11 September 2020;

Published online: 19 October 2020

## References

1. Kruglyak, V. V., Demokritov, S. O. & Grundler, D. Magnonics. *J. Phys. D* **43**, 264001 (2010).

2. Lenk, B. et al. The building blocks of magnonics. *Phys. Rep.* **507**, 107–136 (2011).
3. Krawczyk, M. & Grundler, D. Review and prospects of magnonic crystals and devices with reprogrammable band structure. *J. Phys. Cond. Matter* **26**, 123202 (2014).
4. Chumak, A. V. et al. Magnon spintronics. *Nat. Phys.* **11**, 453–461 (2015).
5. Dieny, B. et al. Opportunities and challenges for spintronics in the microelectronics industry. *Nat. Electron.* **3**, 446–459 (2020).
6. Dubs, C. et al. Sub-micrometer yttrium iron garnet LPE films with low ferromagnetic resonance losses. *J. Phys. D* **50**, 204005 (2017).
7. Dubs, C. et al. Low damping and microstructural perfection of sub-40-nm-thin yttrium iron garnet films grown by liquid phase epitaxy. *Phys. Rev. Mater.* **4**, 024426 (2020).
8. Chumak, A. V., Serga, A. A. & Hillebrands, B. Magnon transistor for all-magnon data processing. *Nat. Commun.* **5**, 4700 (2014).
9. Krivosik, P. & Patton, C. E. Hamiltonian formulation of nonlinear spin-wave dynamics: theory and applications. *Phys. Rev. B* **82**, 184428 (2010).
10. Sadovnikov, A. V. et al. Nonlinear spin wave coupling in adjacent magnonic crystals. *Appl. Phys. Lett.* **109**, 042407 (2016).
11. Khitun, A., Bao, M. & Wang, K. L. Magnonic logic circuits. *J. Phys. D* **43**, 264005 (2010).
12. Manipatruni, S., Nikonov, D. E. & Young, I. A. Beyond CMOS computing with spin and polarization. *Nat. Phys.* **14**, 338–343 (2018).
13. Zografos, O. et al. Design and benchmarking of hybrid CMOS-spin wave device circuits compared to 10-nm CMOS. In *Proceedings of the 15th IEEE International Conference on Nanotechnology* 686–689 (IEEE, 2015).
14. Duan, Z. et al. Nanowire spin torque oscillator driven by spin-orbit torques. *Nat. Commun.* **5**, 5616 (2014).
15. Wang, Q. et al. Spin pinning and spin-wave dispersion in nanoscopic ferromagnetic waveguides. *Phys. Rev. Lett.* **122**, 247202 (2019).
16. Wintz, S. et al. Magnetic vortex cores as tuneable spin-wave emitters. *Nat. Nanotechnol.* **11**, 948–953 (2016).
17. Liu, C. et al. Current-controlled propagation of spin waves in antiparallel, coupled domains. *Nat. Nanotechnol.* **14**, 691–697 (2019).
18. Che, P. et al. Efficient wavelength conversion of exchange magnons below 100 nm by magnetic coplanar waveguides. *Nat. Commun.* **11**, 1445 (2020).
19. Wang, Q. et al. Reconfigurable nanoscale spin-wave directional coupler. *Sci. Adv.* **4**, e1701517 (2018).
20. Kirilyuk, A., Kimel, A. V. & Rasing, T. Ultrafast optical manipulation of magnetic order. *Rev. Mod. Phys.* **82**, 2731 (2010).
21. Kampfrath, T. et al. Coherent terahertz control of antiferromagnetic spin waves. *Nat. Photon.* **5**, 31–34 (2011).
22. Lee, K.-S. & Kim, S.-K. Conceptual design of spin wave logic gates based on a Mach-Zehnder-type spin wave interferometer for universal logic functions. *J. Appl. Phys.* **104**, 053903 (2008).
23. Schneider, T., Serga, A. A. & Hillebrands, B. Realization of spin-wave logic gate. *Appl. Phys. Lett.* **92**, 022505 (2008).
24. Goto, T. et al. Three port logic gate using forward volume spin wave interference in a thin yttrium iron garnet film. *Sci. Rep.* **9**, 16472 (2019).
25. Khivintsev, Y. V. et al. Spin waves in YIG-based networks: logic and signal processing. *Phys. Metals Metallogr.* **120**, 1318–1324 (2019).
26. Fischer, T. et al. Experimental prototype of a spin-wave majority gate. *Appl. Phys. Lett.* **110**, 152401 (2017).
27. Talmelli, G. et al. Reconfigurable nanoscale spin wave majority gate with frequency-division multiplexing. Preprint at <https://arxiv.org/pdf/1908.02546.pdf> (2019).
28. Wu, H. et al. Magnon valve effect between two magnetic insulators. *Phys. Rev. Lett.* **120**, 097205 (2018).
29. Vogt, K. et al. Realization of a spin-wave multiplexer. *Nat. Commun.* **5**, 3727 (2014).
30. Heussner, F. et al. Experimental realization of a passive gigahertz frequency-division demultiplexer for magnonic logic networks. *Phys. Status Solidi* **14**, 1900695 (2020).
31. Papp, A. et al. Nanoscale spectrum analyzer based on spin-wave interference. *Sci. Rep.* **7**, 9245 (2017).
32. Torrejon, J. et al. Neuromorphic computing with nanoscale spintronic oscillators. *Nature* **547**, 428–431 (2017).
33. Brächer, T. & Pirro, P. An analog magnon adder for all-magnonic neurons. *J. Appl. Phys.* **124**, 152119 (2018).
34. Chumak, A. V. in *Spintronics Handbook: Spin Transport and Magnetism* (eds Tsymbal, E. Y. & Žutić, I.) 247–303 (Taylor & Francis, 2019).
35. Sadovnikov, A. V. et al. Directional multimode coupler for planar magnonics: side-coupled magnetic stripes. *Appl. Phys. Lett.* **107**, 202405 (2015).
36. Sebastian, T. et al. Micro-focused Brillouin light scattering: imaging spin waves at the nanoscale. *Front. Phys.* **3**, 35 (2015).
37. Heinz, B. et al. Propagation of spin-wave packets in individual nanosized yttrium iron garnet magnonic conduits. *Nano Lett.* **20**, 4220–4227 (2020).
38. Clausen, P. et al. Mode conversion by symmetry breaking of propagating spin waves. *Appl. Phys. Lett.* **99**, 162505 (2011).

39. Brächer, T., Pirro, P. & Hillebrands, B. Parallel pumping for magnon spintronics: amplification and manipulation of magnon spin currents on the micron-scale. *Phys. Rep.* **699**, 1–34 (2017).
40. Verba, R. et al. Amplification and stabilization of large-amplitude propagating spin waves by parametric pumping. *Appl. Phys. Lett.* **112**, 042402 (2018).
41. Mohseni, M. et al. Parametric generation of propagating spin waves in ultrathin yttrium iron garnet waveguides. *Phys. Status Solidi RRL* **14**, 2000011 (2020).
42. Imre, A. et al. Majority logic gate for magnetic quantum-dot cellular automata. *Science* **311**, 205–208 (2006).
43. Verba, R. et al. Excitation of propagating spin waves in ferromagnetic nanowires by microwave voltage-controlled magnetic anisotropy. *Sci. Rep.* **6**, 25018 (2016).
44. Schneider, M. et al. Bose–Einstein condensation of quasi-particles by rapid cooling. *Nat. Nanotechnol.* **15**, 457–461 (2020).
45. Bauer, H. G. et al. Nonlinear spin-wave excitations at low magnetic bias fields. *Nat. Commun.* **6**, 8274 (2015).
46. Dobrovolskiy, O. V. et al. Spin-wave phase inverter upon a single nanodot. *ACS Appl. Mater. Interfaces* **11**, 17654–17662 (2019).
47. Chen, Y. et al. Parametric resonance of magnetization excited by electric field. *Nano. Lett.* **17**, 572–577 (2017).
48. Sadvonnikov, A. V. et al. Magnon straintronics: reconfigurable spin-wave routing in strain-controlled bilateral magnetic stripes. *Phys. Rev. Lett.* **120**, 257203 (2018).
49. Guillemard, C. et al. Ultralow magnetic damping in Co<sub>2</sub>Mn-based Heusler compounds: promising materials for spintronics. *Phys. Rev. Appl.* **11**, 064009 (2019).
50. Robertson, J. Liquid phase epitaxy of garnets. *J. Cryst. Growth* **45**, 233–242 (1978).
51. Maksymov, I. S. & Kostylev, M. Broadband stripline ferromagnetic resonance spectroscopy of ferromagnetic films, multilayers and nanostructures. *Physica E* **69**, 253–293 (2015).
52. Morozova, M. A. et al. Suppression of periodic spatial power transfer in a layered structure based on ferromagnetic films. *J. Magn. Magn. Mater.* **466**, 119–124 (2018).
53. Vansteenkiste, A. et al. The design and verification of MuMax3. *AIP Adv.* **4**, 107133 (2014).
54. Kumar, D. et al. Numerical calculation of spin wave dispersions in magnetic nanostructures. *J. Phys. D* **45**, 015001 (2012).
55. Venkat, G., Fangohr, H. & Prabhakar, A. Absorbing boundary layers for spin wave micromagnetics. *J. Magn. Magn. Mater.* **450**, 34–39 (2018).

## Acknowledgements

We thank B. Hillebrands for support and valuable discussions. This research has been supported by ERC Starting Grant 678309 MagnonCircuits, FET-OPEN project CHIRON (contract no. 801055), the Deutsche Forschungsgemeinschaft (DFG, German Research Foundation) TRR-173 – 268565370 (Collaborative Research Center SFB/TRR-173 ‘Spin+X’, project B01) and DFG project no. 271741898, the Austrian Science Fund (FWF) through project I 4696-N and the Ministry of Education and Science of Ukraine, project 0118U004007. B.H. acknowledges support from the Graduate School Material Science in Mainz (MAINZ).

## Author contributions

Q.W. proposed the directional coupler and half-adder design, performed the BLS measurements, carried out the evaluation and wrote the first version of the manuscript. C.D. provided the YIG film. M.K., B.H. and B.L. fabricated the nanoscale directional coupler. M.S., B.H. and M.G. developed the BLS set-up. T.B. acquired the SEM micrograph. M.K. performed the VNA-FMR measurements. R.V. developed the analytical theory and performed the theoretical calculations. Q.W. and M.M. performed the micromagnetic simulations. F.C., C.A. and S.D.C. performed the benchmarking and calculated the parameters of the 7-nm CMOS half-adder. O.V.D. and T.B. discussed the interpretation and the relevance of the results. P.P. and A.V.C. led this project. All authors contributed to the scientific discussion and commented on the manuscript.

## Competing interests

The authors declare no competing interests.

## Additional information

**Extended data** is available for this paper at <https://doi.org/10.1038/s41928-020-00485-6>.

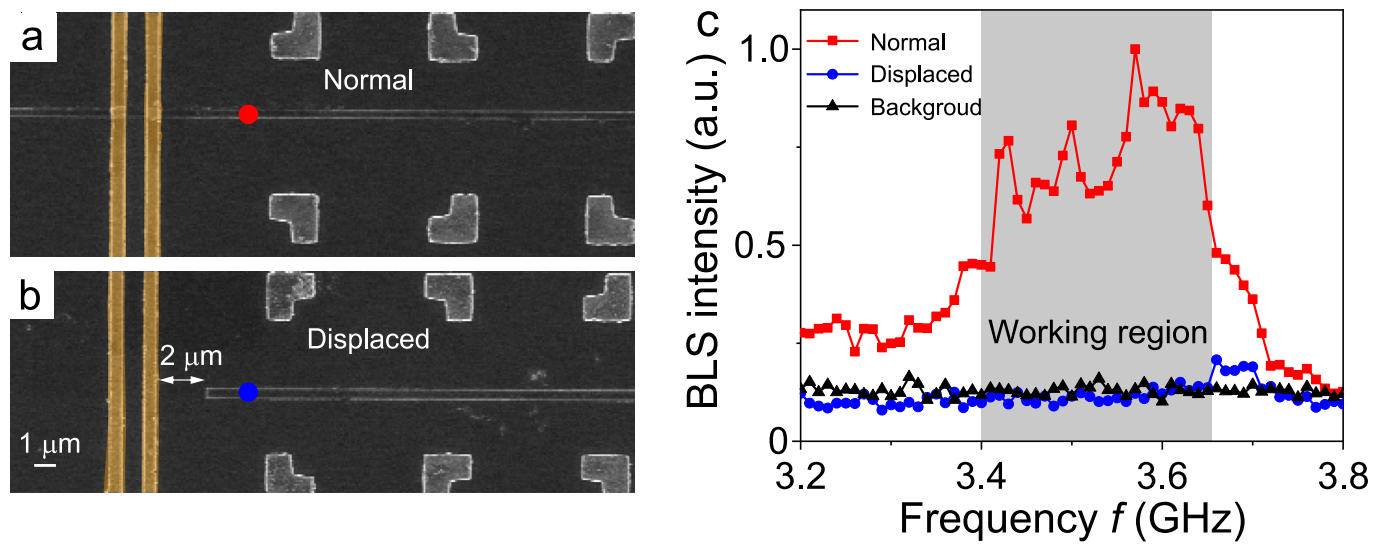
**Supplementary information** is available for this paper at <https://doi.org/10.1038/s41928-020-00485-6>.

**Correspondence and requests for materials** should be addressed to Q.W. or A.V.C.

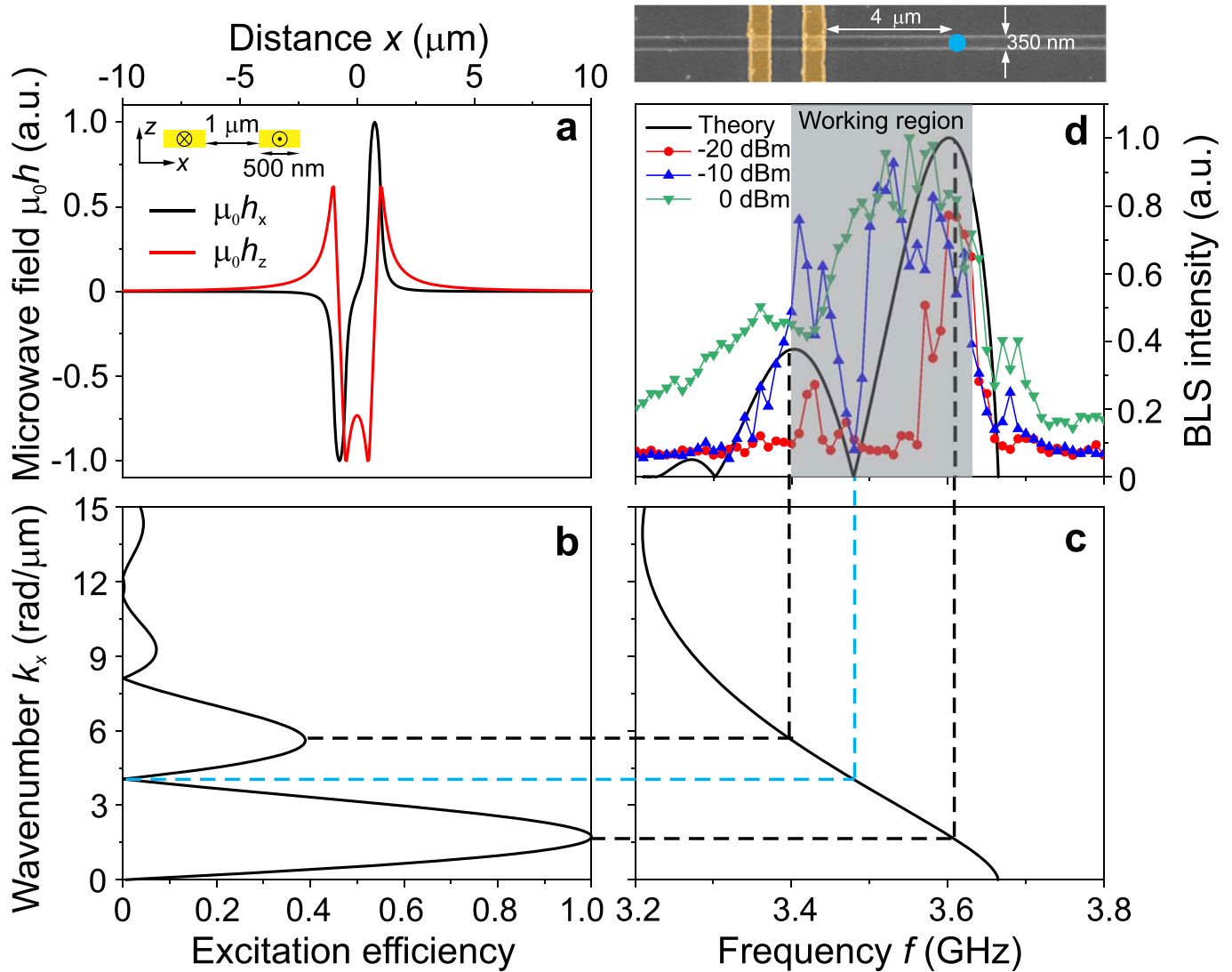
**Reprints and permissions information** is available at [www.nature.com/reprints](http://www.nature.com/reprints).

**Publisher’s note** Springer Nature remains neutral with regard to jurisdictional claims in published maps and institutional affiliations.

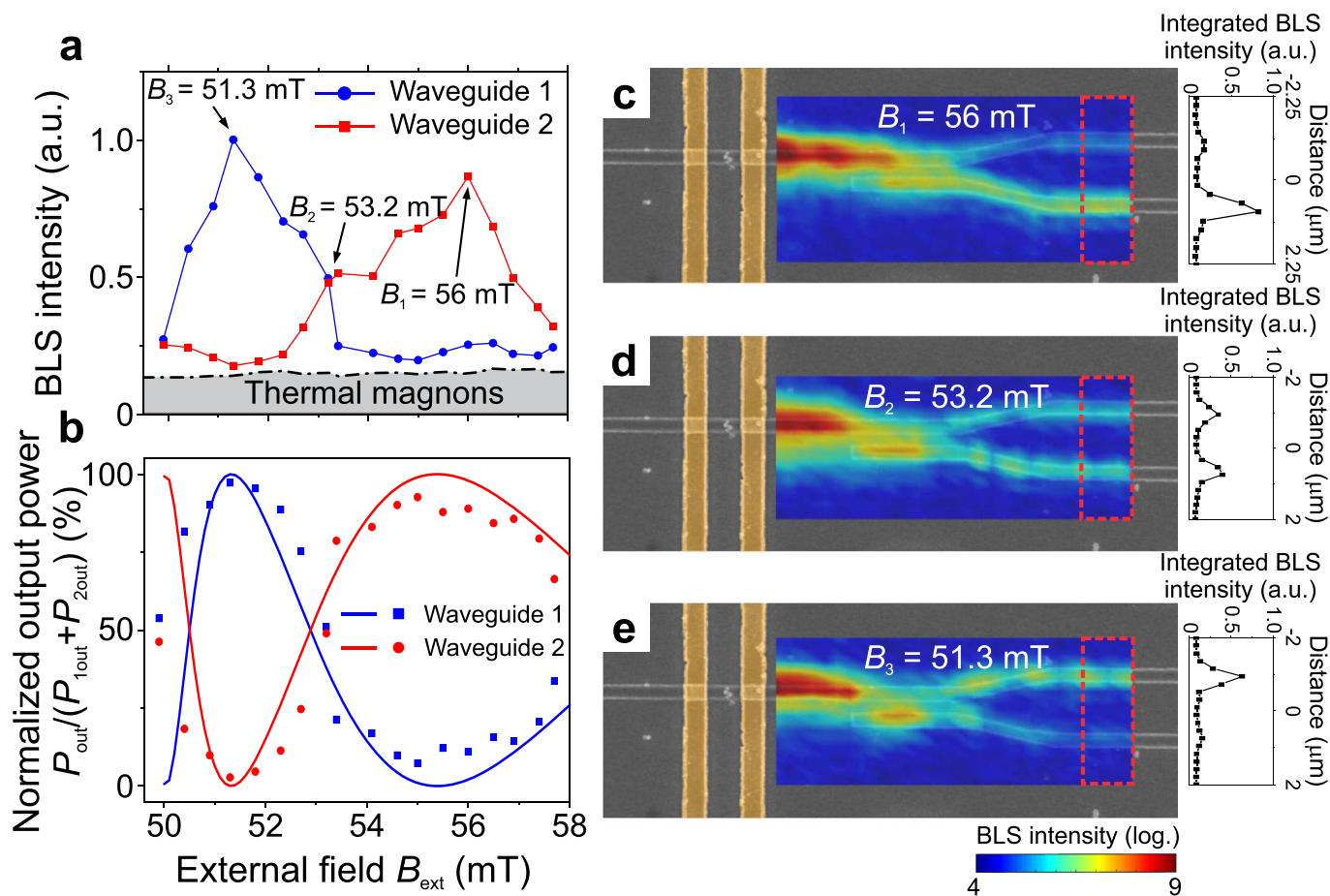
© The Author(s), under exclusive licence to Springer Nature Limited 2020



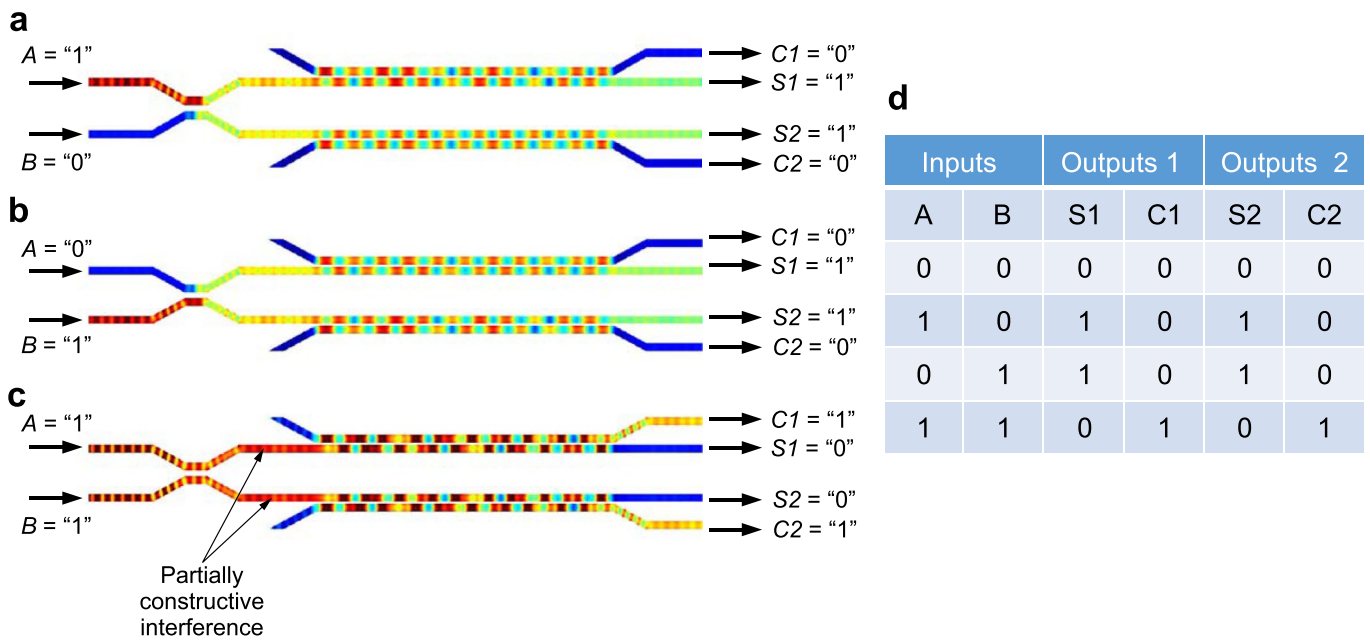
**Extended Data Fig. 1 | Effect of far-field excitation by the U-shaped antenna.** SEM images of the **a** normal and **b** displaced waveguides. The red and blue dots show the  $\mu\text{BLS}$  measurement points. **c**, The spin-wave intensities for normal (red dot line), displaced waveguides (blue dot line) and thermal background (black dot line). The grey area shows the working frequency range in the paper.



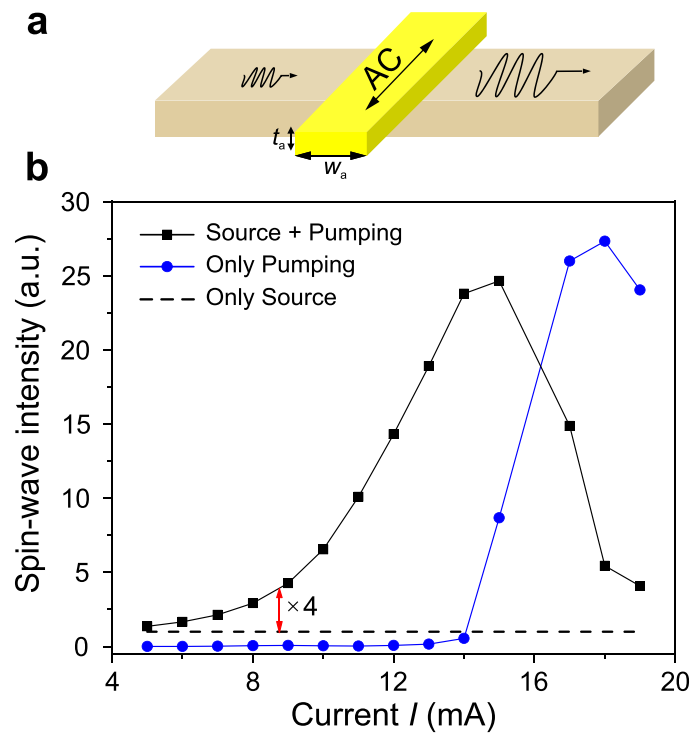
**Extended Data Fig. 2 | Spin-wave spectra in the isolated waveguide.** **a**, The in-plane (black line) and out-of-plane (red line) field distribution created by the U-shape antenna. The schematic cross section of a U-shaped antenna is shown inset. **b**, The excitation efficiency as a function of spin-wave wavenumber. **c**, Spin-wave frequency as a function of spin-wave wavenumber. **d**, Spin-wave intensities are measured 4  $\mu\text{m}$  far from the antenna for different excitation powers. The black line shows the analytical calculation of the spin-wave intensity. A SEM image of the isolated waveguide is shown on the top of Fig. 2d.



**Extended Data Fig. 3 | Reconfigurability of the directional coupler by an applied magnetic field.** **a**, The averaged spin-wave intensity for a frequency of 3.465 GHz as function of the external field for the first (blue circles) and the second (red squares) output waveguide of the directional coupler. **b**, Measured (circles and squares) and theoretically calculated (solid lines) normalized output spin-wave intensities at the first (blue) and second (red) output waveguide for different external fields. **c–e**, Two-dimensional BLS maps of the spin-wave intensity for the different external magnetic fields: **c**,  $B_1 = 56$  mT, **d**,  $B_2 = 53.2$  mT, and **e**,  $B_3 = 51.3$  mT. The right panels show the BLS intensity integrated over the red dashed rectangular regions.



**Extended Data Fig. 4 | Modified half-adder with fan-out gate.** **a-c**, Operational principle and **d** truth table of two half-adders with shared inputs (corresponds to the half-adder with added fan-out logic gate).



**Extended Data Fig. 5 | Parametric amplification.** **a**, A schematic picture of the parametric amplifier. **b**, Output spin-wave intensity as a function of pumping current for different conditions.